LLNL-JRNL-2010484

Lawrence Livermore National Laboratory

Through-Plane Conductive Hydrophobic Electrodes for CO2 Electrolysis to Ethylene

S Elfriede, M Fleischer, H Gross, A Wong, M Goldman, S TzinTzun, J Raisin, E Krall, N Hwee, M Marufu, M Jue, A Sarkar, S Jaffer, S Baker

February 2026

Small

Disclaimer

This work performed under the auspices of the U.S. Department of Energy by Lawrence Livermore National Laboratory under Contract DE-AC52-07NA27344.

Through-Plane Conductive Hydrophobic Electrodes for CO_2 Electrolysis to Ethylene

Eric Krall[1,2], Michell Marufu[1,2], Santiago TzinTzun[1,2,] Melinda L. Jue[1,2], Natalie Hwee[1,2], Shaffiq Jaffer[5], Amitava Sarkar[5,6], Herve Gross[5], Jonathan Raisin[5,6], Maximilian Fleischer[4], Elfriede Simon[4], Sarah Baker[1,2], Andrew A. Wong*[1,3] and Maxwell Goldman*[1,2]

[1]Materials Science Division, Lawrence Livermore National Laboratory, Livermore, CA, USA 94550

[2]Laboratory for Energy Applications for the Future, Lawrence Livermore National Laboratory, Livermore, CA, USA 94550

[3]Materials Engineering Division, Lawrence Livermore National Laboratory, Livermore, CA, USA 94550

[4] Innovation Department, Siemens Energy Global GmbH & Co. KG, Otto-Hahn-Ring 6, Munich 81739, Germany

[5]TotalEnergies Research & Technology USA, LLC, Houston, TX 77002, USA

[6]SUNCAT Center for Interface Science and Catalysis, Department of Chemical Engineering, Stanford University, Stanford, CA 94305, USA

***Correspondence**: goldman23@llnl.gov, wong138@llnl.gov

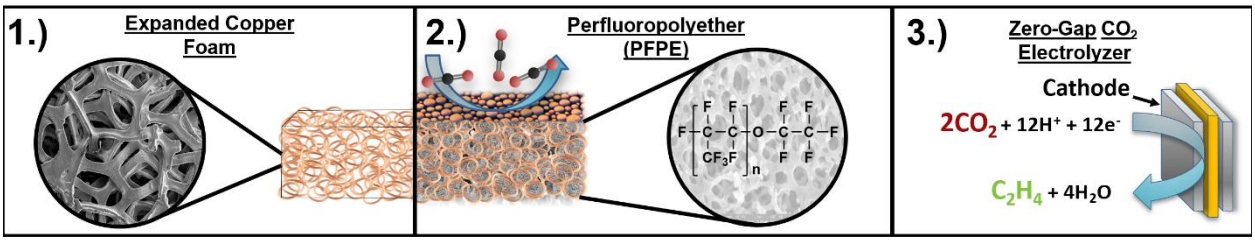

Table of contents figure

Abstract

Copper catalyst gas diffusion electrodes (GDEs) have demonstrated unique electrochemical selectivity converting CO2 to C2-hydrocarbons such as ethylene and ethanol but have been challenged by their hydrophobic chemical stability and internal electrical resistance leading to low energy efficiency. Carbon-supported GDEs have low electrical resistance but lack sufficient stability at industrially relevant current densities. While polymer-supported GDEs have improved hydrophobicity, they also display high in-plane electrical resistance, particularly at industrial scales. In this work, we demonstrate a composite gas diffusion layer that combines hydrophobic porous polymers with an electrically conductive backbone addressing these core gas diffusion electrode

(GDE) scaling challenges. We investigate the material properties of standalone porous perfluoropolyether (PFPE) polymers, including porosity and surface morphology, under varying processing conditions and then incorporate these polymers into a porous copper foam. This composite enhances the mechanical rigidity necessary for cell assembly and provides a through-plane electrical conduction path to reduce electrical resistive losses. This enhanced PFPE composite GDE displays efficient CO2 reduction, achieving 15% ethylene energy efficiency at 100 cm^2. These findings contribute to the development of advanced catalyst materials and electrode architectures and promote scalable strategies for electrochemical conversion of CO_2 into high-value carbon products.

Introduction

Low-temperature electrochemical carbon dioxide reduction (eCO_2R) is an emerging technology that can expand domestic feedstocks for manufacturing fuels and commodity chemicals[1]. Copper (Cu) based catalysts for eCO_2R produce a wide range of carbon products including carbon monoxide, formate, methane, ethanol, ethylene and acetate[2,3]. Recent advances in CO_2-to-C_1 (single carbon molecules) electrolyzers have demonstrated readiness for scale-up and private sector investment[4]. However, advancing the commercial viability of CO_2 electrolysis to ethylene requires significant increases in energy efficiency, ethylene Faradaic efficiency, and long-term operation[5–7].

One strategy to mitigate ohmic losses and improve energy efficiency for CO_2 electrolysis systems is to use a zero-gap membrane electrode assembly (MEA). Within this architecture, gas diffusion layers (GDLs) are constrained to allow either through-plane electrical conduction, as seen in carbon-based scaffolds that facilitate electron transfer[8], or to provide enhanced hydrophobicity, such as PTFE-based porous supports that resist flooding. Electrically conductive GDLs require hydrophobic coatings to mitigate flooding[8–11]. Several strategies exist for making the cathode GDL hydrophobic including treating carbon-based electrodes with polymers such as polytetrafluoroethylene (PTFE)[8] or combining PTFE with the catalyst layer that is deposited on top of carbon-based electrodes[12]. Recent demonstrations show that using carbon-based gas diffusion layers in zero-gap electrolyzers for ethylene can achieve 300 mA cm^{-2} at 5 cm^2 for 40 hours[13] and up to 200 hours at 100 cm^2 geometric area[14]. However, these CO_2-to-ethylene durability experiments are significantly shorter in duration than recent CO_2 to CO demonstrations because the PTFE used in carbon-based electrodes for CO_2-to-ethylene electrolysis can be insufficient to prevent flooding which results in loss of stability and performance[10,15,16]. Using highly hydrophobic materials in cathodes designed for CO_2 conversion to ethylene is particularly important because these electrochemical systems also produce low surface tension liquid products such as ethanol; the lower liquid surface tension makes it more likely that the cathode will flood, preventing CO_2 transport to the catalyst surfaces.[17,18].

Research on eCO_2R indicates that substituting carbon-based electrodes with porous, hydrophobic GDLs (such as expanded PTFE) for Cu-based electrodes can achieve high Faradaic efficiencies for C_{2+} (multi-carbon molecule) products while enabling stable and continuous operation in single-gap electrolyzers[19–21]. However, a tradeoff of using PTFE-based catalysts supports is the need to rely entirely on in-plane electrical conductivity. This leads to poor energy efficiency due to modest in-plane conductivity and lack of through-plane electrical conduction[22,23]. This limitation is exacerbated by inefficient electrical contact and long conduction paths leading to high electrical resistance. Therefore, there is a need to develop material that combines the through-plane conductivity of

carbon-based electrodes with the enhanced selectivity and stability of hydrophobic polymer-supported catalysts.

In this work, we present the development of a composite GDE composed of macro-porous copper foam infused with a hydrophobic, micro-porous perfluoropolyether (PFPE) polymer (Figure 1). The porous PFPE polymer can be fabricated with a range of permeabilities and porosities, influenced by variations in curing light intensity and monomer loading in the formulation. While the PFPE polymer has previously demonstrated high selectivity for carbon products such as ethylene in a 3-D printed 1.5 cm^2 flow-cell reactor system[24], it lacks through-plane conductivity and, on its own, does not have the mechanical properties to maintain structural integrity in a zero-gap electrolyzer. Our composite GDE leverages the structurally-tunable, hydrophobic properties of porous PFPE polymers and the highly conductive, mechanically rigid structure of copper foams to enable efficient, scalable CO_2 electrolysis in a zero-gap architecture, exhibiting 15% energy efficiency toward ethylene for 4 hours at 100 cm^2.

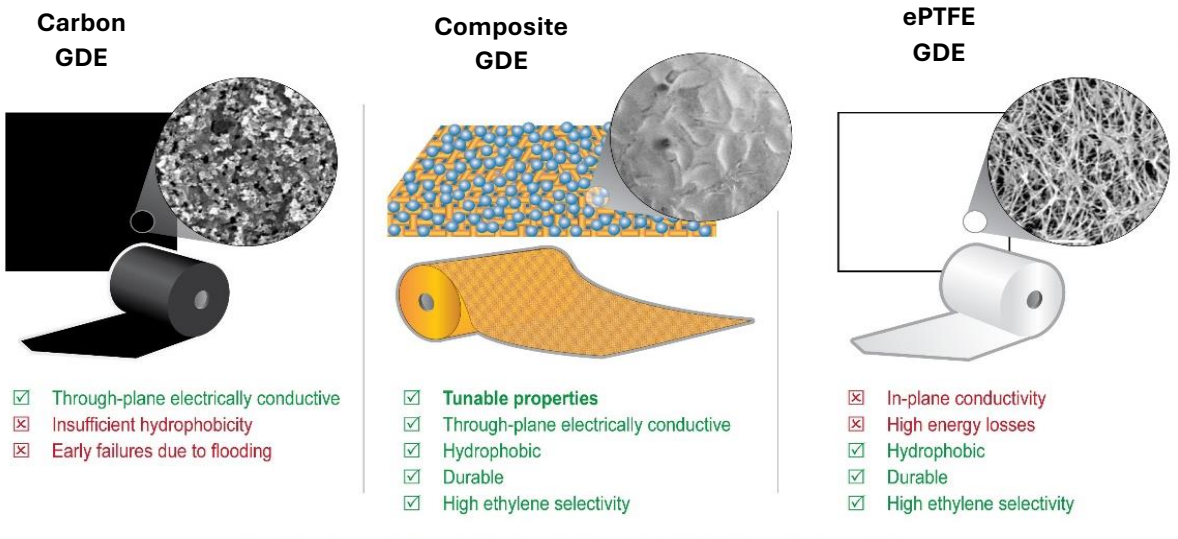

Figure 1: Comparison of the advantages and limitations of carbon gas diffusion electrodes (GDEs), porous polymer-foam composite GDEs, and expanded PTFE GDEs for electrochemical CO_2 reduction applications.

Results and Discussion

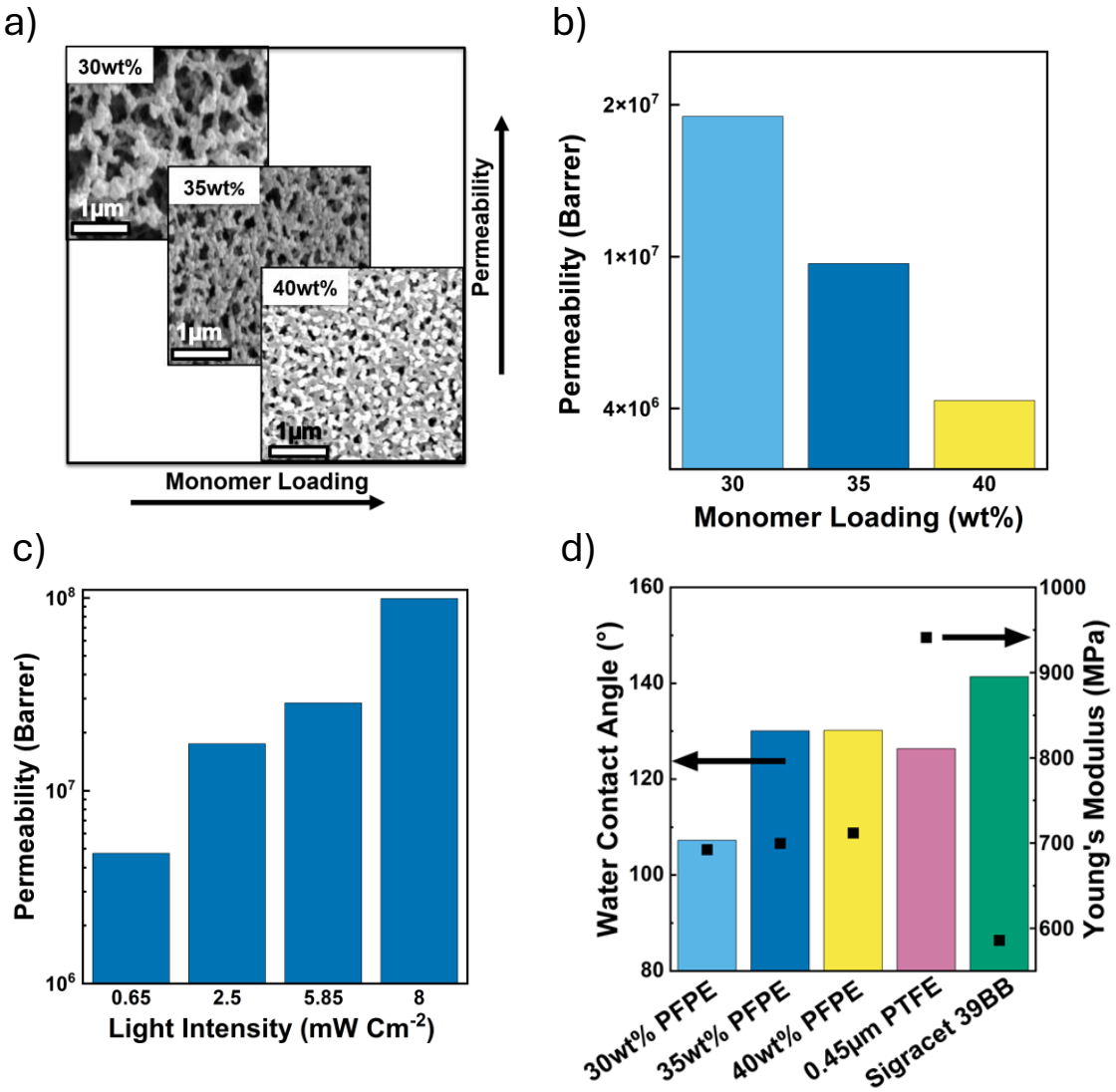

Figure 2: Physical characterization of free-standing, porous PFPE polymers. (a) Relationship between resin monomer loading and gas permeability for porous PFPE cured at 5.85 mW/cm^2. (b) SEM images of the cured, porous PFPE polymers with different resin formulation monomer loadings. (c) Relationships between curing UV light intensity and gas permeability for 35 wt% PFPE polymer loading. (d) Mechanical force-displacement relationship and water contact angle for different weight percent PFPE polymers compared to standard carbon-based (Sigracet® 39BB), and (e-PTFE-based gas diffusion layer supports.

Building on the approach established by Wicks et al.[24], we formulated our PFPE matrix using a ternary mixture: a hydrophobic, dimethacrylate-functionalized PFPE monomer and two non-reactive porogenic agents. By tuning the monomer-to-porogen ratios to the cloud point phase, we achieved a phase-separated microstructure upon UV curing, resulting in a highly porous, interconnected polymer network (Figure 2a). This formulation yielded membranes with gas permeance and hydrophobicity comparable to commercial ePTFE, while enabling precise control over pore morphology and mechanical integrity critical for scalable GDE fabrication.

One of the advantages of using a porous PFPE composite as the hydrophobic gas diffusion element in these electrodes is the ability to create a range of microporous properties by adjusting the resin

formulation and curing conditions. We systematically varied the PFPE monomer loading (30–40 wt%) in the photocurable resin and the UV irradiation intensity (0.65–8 mW cm^{-2}) at a fixed dose of 150 mJ cm^{-2}. Stand-alone porous PFPE polymer materials 150µm thick were first prepared and characterized without Cu-foam support to isolate the polymer network behavior. We characterized CO_2 permeability, water contact angle, Young's modulus, and pore morphology to understand the range of structural, transport, and interfacial properties of these porous PFPE polymers, and to map out the processing window for viable gas diffusion layers (Figure 2).

The PFPE monomer loading is the variable that has the greatest impact on pore network density, pore architecture, and the mechanical integrity of the cured porous PFPE polymer. As the resin content of PFPE increases from 30 wt% to 40 wt%, gas permeability of the cured porous PFPE polymer decreases by nearly and order of magnitude (Figure 2b). This trend is attributed to a greater volume fraction of PFPE in the cured porous polymer and therefore a tighter PFPE crosslinking density (Table SI 1), which leads to smaller pores and a greater fraction of gas-impermeable pore space. Scanning electron microscope (SEM) micrographs in Figure 2a reveal a transition from an open, highly reticulated pore network at 30 wt%, which supported high CO_2 flux, to a more closed-pore morphology at 40 wt%, where decreased interconnectivity constricts or fully block gas transport. At loadings below 30 wt%, cured PFPE polymers are also easily torn even with careful handling due to insufficient crosslinking density. In contrast, materials exceeding 40 wt% PFPE are brittle, with observable cracking when modestly compressed in a zero-gap electrolyzer (Figure SI 1). Further hotpressing of the porous cured PFPE polymer led to collapsing of the pores structure rendering it unsuitable as a gas diffusion layer (Figure SI 2). When porous, PFPE polymers from 35 wt% PFPE resins exhibit moderate gas permeability and can be manipulated by hand. These results indicate an ideal range of PFPE monomer loading that can yield practical porous transport layers for electrochemical devices.

Using 35 wt% PFPE loading as the standard resin composition, we explored the impact of photocuring UV light intensity on CO_2 transport through the stand-alone porous PFPE polymer. Holding the total UV dose constant at 150 mJ cm^{-2}, we varied the irradiation intensity from 0.65 mW cm^{-2} to 8 mW cm^{-2}. CO_2 permeability increases with increased photocuring light intensity (Figure 2c), reflecting a rapid radical-mediated crosslinking that preserves microporous channels. However, above 6 mW cm^{-2}, SEM micrographs revealed a dense, skin-like polymer layer interrupted by isolated macroporous defects (Figure SI 3). These micrographs indicate that while higher UV light intensity accelerates polymerization and increases overall permeability, it can also introduce manufacturing artifacts resulting in nonuniform pore distribution, increased volumetric shrinkage, and impermeable skin-layers. These effects diminish mechanical integrity and pore connectivity, ultimately compromising membrane quality and reproducibility. Because of this, a curing intensity between 3 mW cm^{-2} and 6 mW cm^{-2} emerges as a viable processing window for promoting uniform interpenetrating pore networks.

In addition to gas permeability, GDLs for CO_2 electrolysis must exhibit durable hydrophobicity to prevent flooding of the cathode catalyst layer and mechanical integrity to endure the compressive forces during assembly and operation in a zero-gap electrolyzer. Using a photocuring UV light intensity of 5.85 mW cm^{-2}, we evaluated the hydrophobicity and compressive strength of the porous PFPE polymers using contact angle goniometry and Instron® compression testing respectively. We measured the static water contact angle of porous 35 wt% PFPE polymer to be 135° (Figure 2d),

which falls between PTFE-treated carbon paper (140°) and ePTFE membranes (125°), which are typical hydrophobic materials use for sustained CO_2 electrolysis. Compression testing yielded a Young's modulus of about 700 MPa, showing a compressive stiffness that is higher than commercially available PTFE-treated carbon papers and that is lower than ePTFE. Through tuning the fabrication process, we can produce porous PFPE polymers that closely match ePTFE in CO_2 permeability while exhibiting hydrophobicity and mechanical stiffness that fall between ePTFE and Sigracet® 39BB carbon paper.

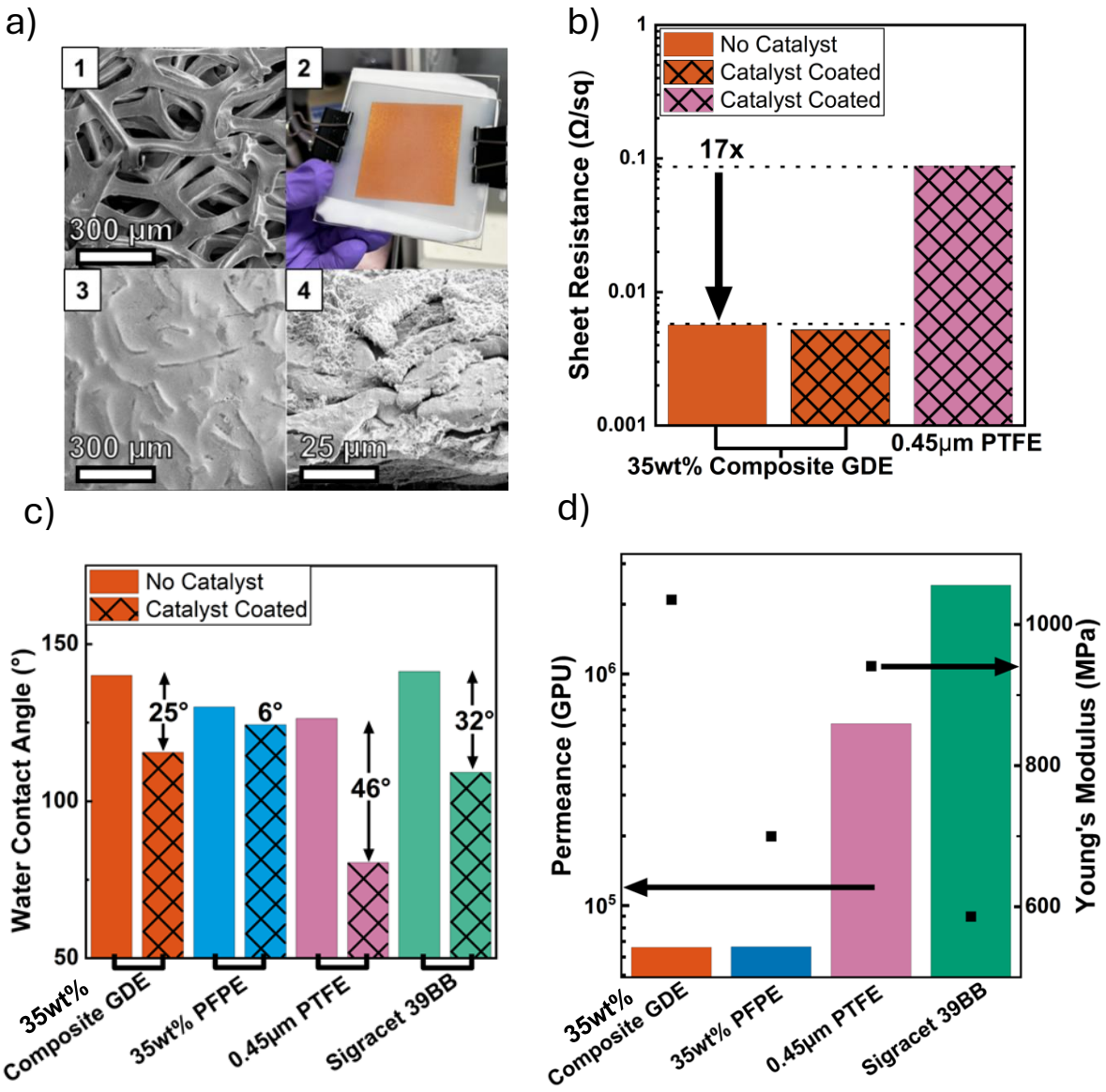

Figure 3: Physical characteristics of copper foam infilled with porous PFPE polymer. (a) images of (1) stand-alone copper foam (SEM micrograph). (2) preparation of copper foam, fully saturated with PFPE resin and sandwiched between glass slides (photograph). SEM micrographs of (3) copper foam infilled with cured 35 wt% porous PFPE polymer and (4) cross sectional view of the copper foam/porous PFPE polymer composite. (b) Electrical sheet resistances of copper foam/porous PFPE polymer composite, both coated and uncoated with a copper catalyst, and a comparable copper catalyst on a 0.45

μm ePTFE support. (c) Water contact angle of uncoated and copper catalyst coated gas diffusion layer substrates. (d) Young's modulus and gas permeance of copper foam/porous PFPE polymer composites compared to standalone PFPE, ePTFE, and Sigracet® 39BB carbon paper.

By infilling a macroporous copper foam with PFPE resin followed by UV-induced polymerization, we produce a composite GDE that combines many of the desirable properties of both the conductive metal and the hydrophobic polymer. Figure 3a shows the resin infusion and UV-cure workflow, where copper foam (Figure 3a-1), which exhibits high electrical conductivity, is saturated with PFPE resin (Figure 3a-2) before UV curing and subsequent supercritical CO_2 drying to yield the final composite material (Figure 3a-3). Cross-sectional SEM micrographs (Figure 3a-4 and Figure SI 4,5) show a uniform PFPE coating on Cu struts while preserving the open-cell pores necessary for gas transport. Four-point probe measurements indicate that the Cu-foam/PFPE composite retains an electrically conductivity network in addition to the in-plane conductivity of a 500 nm copper catalyst coating. This results in a 17x reduction in sheet resistance compared to a catalyst-coated ePTFE as seen in Figure 3b. Because of the electrically conductive network of the copper foam, the composite samples also exhibit through plane conductivity, regardless of catalyst coating, with 7x lower measured resistance in a zero-gap cell compared to carbon paper (Figure SI 6).

Gas transport and wettability analyses of the copper foam/porous PFPE polymer composite indicate that the mechanical, chemical, and electrical enhancements of each component incur only minor tradeoffs when combined into a full structure. CO_2 permeance of the composite GDE (Figure 3d) differs by just 0.5% compared to standalone porous PFPE polymer, with a permeance of 6.61×10^4 Barrer and 6.64×10^4 Barrer respectively. The compressive Young's modulus is much higher, ~1.0 GPa, which increases resistance to pore collapse under the compressive loads experienced during the assembly and operation of the electrochemical cell. Both composite and stand-alone PFPE polymers coated with catalyst exhibit higher static water contact angles compared to catalyst-coated expanded PTFE and carbon paper (Figure 3c) suggesting that the starting surface morphology and pore uniformity might contribute to catalyst growth preferential to higher hydrophobicity. By coating copper catalysts on copper foam infilled with porous PFPE polymer, we can produce a composite GDE that uniquely integrates high CO_2 permeability, persistent hydrophobicity, enhanced compressive stiffness, and electrical through-plane connectivity.

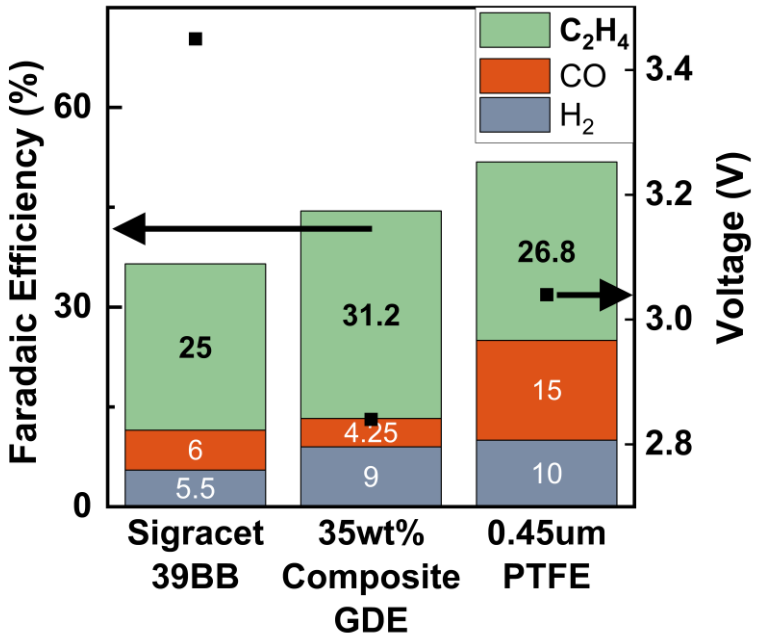

Figure 4: Gas selectivity of various 25 cm^2 electrodes in a zero-gap CO_2 electrolyzer.

We evaluated the Cu foam/PFPE polymer composite GDE in a 25 cm^2 zero-gap CO_2 electrolyzer and compare this to identical experiments using copper-coated Sigracet® (39BB) and ePTFE respectively as cathode GDEs (figure 4). Cross sections of the electrodes can be seen in Figure SI 7. All experiments used a Sustainion® Grade T ion exchange membrane, a Ni foam anode, 3 L of 0.5 M CsOH anolyte, humidified CO_2 gas at a flow rate of 180 sccm, 40 °C cell temperature, and gas/liquid back pressures of 20 psi. Benchmarking electrochemical performance was performed at 25 cm^2 to demonstrate scalability of the composite electrode at industrially relevant current densities (200 mA cm^{-2}). At a fixed current density 200 mA cm^{-2}, the composite electrode displayed an ethylene Faradaic efficiency (FE) of ~31%, the highest among samples tested with the Grade T membrane. Using a Sustainion™ Grade RT membrane and 0.5 M KOH as the anolyte we achieved $F.E._{ethylene}$ of 34% (2.5 V) at 20 psi and 40.5% (2.58) at 10 psi gas/liquid back pressure (Figure SI 8). Liquid-phase CO_2 reduction products, including alcohols such as ethanol and carbon-based ions such as formate, exit the cell predominantly by crossing the membrane and entering the anolyte, but can also pass through the cathode GDL, borne by water and water vapor, and condense at the CO_2 gas outlet; the latter is difficult to accurately quantify due to the high humidity of the inlet CO_2 gas and the inability to accurately quantify water crossover. Because of this, we determine liquid product Faradaic efficiencies by performing HPLC on anolyte samples. Furthermore, we perform a full product analysis of similar tests at 100 cm^2 using a Sustainion® Grade RT membrane (Figure SI 9) to support the results of measuring liquid products from the anolyte. This high ethylene selectivity (>30%) in a zero-gap reactor with unoptimized catalyst layer structure or operating conditions represents a baseline performance for this novel electrode architecture. Post-mortem analysis of the cathodes were not performed due to significant delamination of the catalyst layer as well as transference of the membrane to the cathode electrode (Figure SI 10).

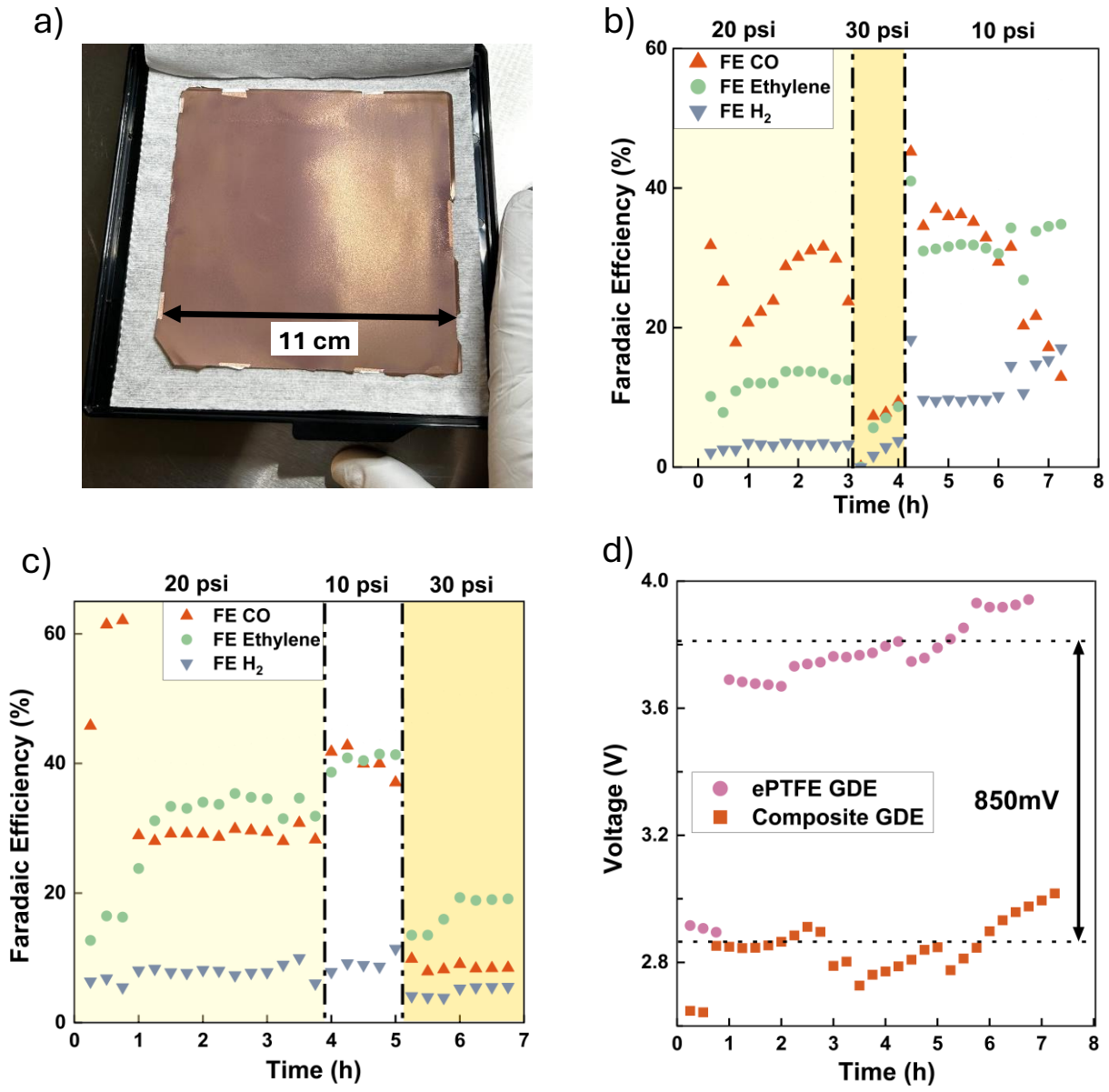

Figure 5: Electrochemical performance of 100 cm² composite GDE and ePTFE GDE. (a) Scaled up 35 wt% composite GDE after 500 nm catalyst coating. (b) 100 cm² 35 wt% composite GDE 8-hour electrochemical operation at 200 mA/cm² over 3 pressure changes. (c) 100 cm² 1 µm ePTFE GDE 8-hour electrochemical operation at 200 mA/cm²over 3 pressure changes. (d) Operating cell voltage comparison of 35 wt% composite GDE and 1µm ePTFE GDE over 8 hours of electrochemical operation.

To highlight the scalability and durability of these architected cathodes, we manufactured 100 cm^2 geometric area composite GDEs (Figure 5a) and performed 8-hour constant-current CO_2 electrolysis (Figure 5b), incorporating modulation of the gas/liquid back pressures. We compared our composite GDE to a reference case: a 1 µm pore-size ePTFE GDE at 100 cm^2 (Figure 5c). Water breakthrough pressure measurements confirmed that the composite GDE exhibits relatively low breakthrough pressure, comparable to the 1 µm ePTFE (Figure SI 11). For additional context, we tested 0.45 µm

pore-size ePTFE GDEs (Figure SI 12), which showed a stepwise decrease in ethylene Faradaic efficiency after successive anolyte swaps. These smaller-pore GDEs (0.45 μm vs 1 μm) did not provide a suitable comparison point due to excess water accumulation at the Cu catalyst surface resulting from their higher water breakthrough pressures, as previously reported[25]. All electrochemical testing at 100 cm^2 utilized a Sustainion® grade RT membrane, Ni foam anode, 200 mA cm^{-2}, 5 L of 0.5 M CsOH anolyte, and 40 °C cell temperature.

Assessing the Faradaic efficiencies for ethylene, CO, and hydrogen over an 8 hour experiment (Figure 5b), we observe a peak ethylene FE of ~33 % while maintaining ≤ 3 V full cell voltage with a back pressure of 10 psi. Occasional anolyte swaps of fresh 5 L 0.5 M CsOH occurred throughout the experiments to maintain a pH at the anode >13 to prevent Ni dissolution. The discontinuous product distribution trends stem from step changes in cell pressure. At 20 psi back pressure, selectivity for CO is favored over ethylene with minimal hydrogen production. Raising the pressure to 30 psi suppresses all gas products with the anticipated tradeoff of promoting liquid product production. Lowering the pressure to 10 psi increases the Faradaic efficiency for both ethylene and CO, accompanied by a 10% increase in hydrogen Faradaic efficiency. We chose to use a different pressure sequence for the two tests to confirm that the change in product distribution was related to the back pressure of the system and independent of time. A full liquid product analysis for the experiment depicted in Figure 5b is presented in Figure SI 5. We hypothesize that these variations in product selectivity reflect pressure-induced changes in local pH, surface potential, and the surface coverage ratio of CO_2 to CO. With these small adjustments in the operating parameters, we were able to achieve similar ethylene Faradaic efficiency and full cell voltage when scaling from a geometric area of 25 cm^2 to 100 cm^2. While the ePTFE GDE achieved slightly higher ethylene and lower hydrogen Faradaic efficiencies (Figure 5c), it also displayed a markedly higher average full cell voltage (Figure 5d), highlighting one of the advantages of our low-resistance through-plane conductive composite GDE, particularly when scaling towards industrially relevant electrode surface areas. Technoeconomic analysis of CO_2 electrolyzers indicates that the cost of electricity is the primary driver in the overall cost of the unit. Recent TEAs suggest that the cost of the copper cathode can be ignored in electrolyzer costs due to negligible contributions compared to the cost of IrO_2 and commercial AEMs.[26] The cost of the copper foam is 1.3x the cost of Sigracet 39BB which suggests that the cost of the composite electrode will be comparable to carbon paper. We contend that the benefit of the composite GDE is due to the increase in energy efficiency at 100 cm^2 (14.0%) compared to the ePTFE electrode (12%). Figure 6 shows a comparison of the energy efficiency of our composite GDE compared to other demonstrations of CO_2 to ethylene at >= 25 cm^2 (Table S2).

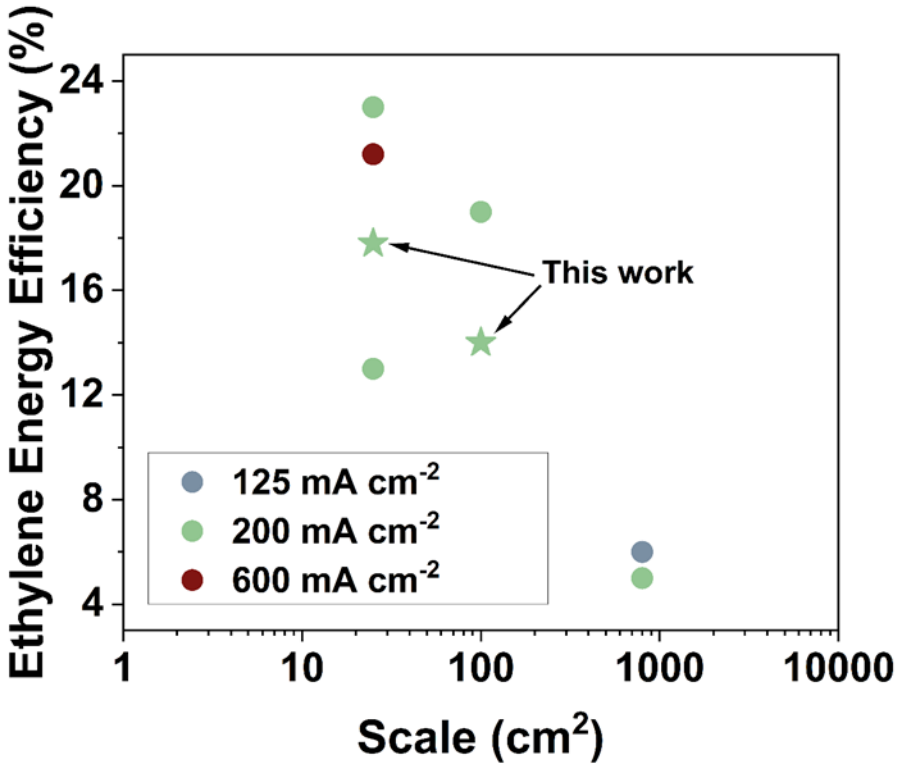

Figure 6. Comparison of energy efficiency for electrochemical CO_2 to ethylene at scales >25 cm^2.[27,28,29,30,31,32]

Conclusions

In this work, we present an electrically conductive, hydrophobic metal-polymer composite electrode designed for carbon dioxide electrolysis systems to address the chemical stability and electrical conduction limitations of typical gas diffusion electrodes. This composite gas-diffusion layer features a macroporous copper-foam scaffold infilled with a microporous perfluoropolyether (PFPE) polymer. By tuning the starting PFPE concentration in the photocurable resin and varying the polymer curing conditions, we demonstrate control over both the polymer microstructure and physical properties. In a zero-gap electrochemical cell to convert carbon dioxide to ethylene, the composite gas diffusion electrode exhibits >30% Faradaic efficiency and 15% energy efficiency at 100 cm^2 for 4 hours. This composite electrode offers unique opportunities by tuning material properties and mitigating flooding in the porous transport layer allowing for improvements in catalyst layer development. Future optimization of the electrode structure, understanding the impact of pressure on selectivity and improvements in the catalyst layer offers a unique opportunity to further improve performance and aid in conforming hydrophobic electrodes to existing electrolyzer hardware for rapid deployment at industrial scales.

Acknowledgements

M.G., E.K., M.M., M.J., S.T., N.H., A.A.W., S.B. acknowledge financial support from TotalEnergies SE, and Siemens-Energy SE. This material is based upon work supported by the U.S. Department of Energy's Office of Energy Efficiency and Renewable Energy (EERE) under the Advanced Manufacturing Office (AMO) funding opportunity announcement DE-FOA-0002252. E.K., M.M., S.T., M.J., N.H., S.B., A.A.W., M.G contributed under the auspices of the US Department of Energy by Lawrence Livermore National Laboratory under contract DE-AC52-07NA27344 within CRADA TC02449, IM: LLNL-JRNL-2010484. We acknowledge the help from the LLNL Program Development Support Office in creating Figure 1.

Author Contributions

E.K. conceptualized the composite GDE, carried out experiments, contributed to the discussion, and prepared the manuscript. M.M. carried out electrochemical experiments, contributed to the discussion and edited the manuscript. S.T, M.L.J, N.H, carried out experiments, contributed to the discussion and edited the manuscript. S.J., A.S., H.G., J.R., M.F., E.F., S.B. contributed to the discussion and edited the manuscript. A.A.W. supervised the project, contributed to the discussion and prepared the manuscript. M.G. supervised the project, carried out electrochemical experiments, contributed to the discussion, conceptualized the composite GDE, and prepared the manuscript.

Competing Interests

The authors have a U.S. patent application for the composite electrode described within the manuscript.

References:

(1) Guerra, O. J.; Almajed, H. M.; Smith, W. A.; Somoza-Tornos, A.; Hodge, B.-M. S. Barriers and Opportunities for the Deployment of CO2 Electrolysis in Net-Zero Emissions Energy Systems. *Joule* **2023**, *7* (6), 1111–1133. https://doi.org/10.1016/j.joule.2023.05.002.

(2) Lee, M.-Y.; Park, K. T.; Lee, W.; Lim, H.; Kwon, Y.; Kang, S. Current Achievements and the Future Direction of Electrochemical CO_2 Reduction: A Short Review. *Crit. Rev. Environ. Sci. Technol.* **2020**, *50* (8), 769–815. https://doi.org/10.1080/10643389.2019.1631991.

(3) Lin, J.; Zhang, Y.; Xu, P.; Chen, L. CO2 Electrolysis: Advances and Challenges in Electrocatalyst Engineering and Reactor Design. *Mater. Rep. Energy* **2023**, *3* (2), 100194. https://doi.org/10.1016/j.matre.2023.100194.

(4) Goldman, M.; Prajapati, A.; Duoss, E.; Baker, S.; Hahn, C. Bridging Fundamental Science and Applied Science to Accelerate CO2 Electrolyzer Scale-Up. *Curr. Opin. Electrochem.* **2023**, *39*, 101248. https://doi.org/10.1016/j.coelec.2023.101248.

(5) Shin, H.; Hansen, K. U.; Jiao, F. Techno-Economic Assessment of Low-Temperature Carbon Dioxide Electrolysis. *Nat. Sustain.* **2021**, *4* (10), 911–919. https://doi.org/10.1038/s41893-021-00739-x.

(6) Moore, T.; Oyarzun, D. I.; Li, W.; Lin, T. Y.; Goldman, M.; Wong, A. A.; Jaffer, S. A.; Sarkar, A.; Baker, S. E.; Duoss, E. B.; Hahn, C. Electrolyzer Energy Dominates Separation Costs in State-

of-the-Art CO2 Electrolyzers: Implications for Single-Pass CO2 Utilization. *Joule* **2023**, *7* (4), 782–796. https://doi.org/10.1016/j.joule.2023.03.015.
(7) Chapter 10. Electrochemical Reactors. In *Energy and Environment Series*; Royal Society of Chemistry: Cambridge, 2020; pp 408–432. https://doi.org/10.1039/9781788015844-00408.
(8) Yang, K.; Kas, R.; Smith, W. A.; Burdyny, T. Role of the Carbon-Based Gas Diffusion Layer on Flooding in a Gas Diffusion Electrode Cell for Electrochemical CO_2 Reduction. *ACS Energy Lett.* **2021**, *6* (1), 33–40. https://doi.org/10.1021/acsenergylett.0c02184.
(9) Moss, A. B.; Garg, S.; Mirolo, M.; Giron Rodriguez, C. A.; Ilvonen, R.; Chorkendorff, I.; Drnec, J.; Seger, B. In Operando Investigations of Oscillatory Water and Carbonate Effects in MEA-Based CO2 Electrolysis Devices. *Joule* **2023**, *7* (2), 350–365. https://doi.org/10.1016/j.joule.2023.01.013.
(10) Leonard, M. E.; Clarke, L. E.; Forner-Cuenca, A.; Brown, S. M.; Brushett, F. R. Investigating Electrode Flooding in a Flowing Electrolyte, Gas-Fed Carbon Dioxide Electrolyzer. *ChemSusChem* **2020**, *13* (2), 400–411. https://doi.org/10.1002/cssc.201902547.
(11) Jeanty, P.; Scherer, C.; Magori, E.; Wiesner-Fleischer, K.; Hinrichsen, O.; Fleischer, M. Upscaling and Continuous Operation of Electrochemical CO2 to CO Conversion in Aqueous Solutions on Silver Gas Diffusion Electrodes. *J. CO2 Util.* **2018**, *24*, 454–462. https://doi.org/10.1016/j.jcou.2018.01.011.
(12) Xing, Z.; Hu, L.; Ripatti, D. S.; Hu, X.; Feng, X. Enhancing Carbon Dioxide Gas-Diffusion Electrolysis by Creating a Hydrophobic Catalyst Microenvironment. *Nat. Commun.* **2021**, *12* (1). https://doi.org/10.1038/s41467-020-20397-5.
(13) Wang, L.; Chen, Z.; Xiao, Y.; Huang, L.; Wang, X.; Fruehwald, H.; Akhmetzyanov, D.; Hanson, M.; Chen, Z.; Chen, N.; Billinghurst, B.; Smith, R. D. L.; Singh, C. V.; Tan, Z.; Wu, Y. A. Stabilized Cuδ+-OH Species on in Situ Reconstructed Cu Nanoparticles for CO2-to-C2H4 Conversion in Neutral Media. *Nat. Commun.* **2024**, *15* (1), 7477. https://doi.org/10.1038/s41467-024-52004-2.
(14) Xiao, Y.; Yu, F.; Xia, C.; Zhu, D.; Chen, J.; Liu, N.; Zhao, Y.; Qi, R.; Guo, W.; You, B.; Yao, T.; Pang, Y.; Wang, Z.; Wang, H.; Song, F.; Xia, B. Y. Asymmetric CO–CHO Coupling over Pr Single-Atom Alloy Enables Industrial-Level Electrosynthesis of Ethylene. *J. Am. Chem. Soc.* **2025**, *147* (18), 15654–15665. https://doi.org/10.1021/jacs.5c02896.
(15) Iglesias Van Montfort, H.-P.; Li, M.; Irtem, E.; Abdinejad, M.; Wu, Y.; Pal, S. K.; Sassenburg, M.; Ripepi, D.; Subramanian, S.; Biemolt, J.; Rufford, T. E.; Burdyny, T. Non-Invasive Current Collectors for Improved Current-Density Distribution during CO2 Electrolysis on Super-Hydrophobic Electrodes. *Nat. Commun.* **2023**, *14* (1). https://doi.org/10.1038/s41467-023-42348-6.
(16) Hao, S.; Elgazzar, A.; Zhang, S.-K.; Wi, T.-U.; Chen, F.-Y.; Feng, Y.; Zhu, P.; Wang, H. Acid-Humidified CO2 Gas Input for Stable Electrochemical CO2 Reduction Reaction. *Science 388* (6752), eadr3834. https://doi.org/10.1126/science.adr3834.
(17) Leonard, M. E.; Orella, M. J.; Aiello, N.; Román-Leshkov, Y.; Forner-Cuenca, A.; Brushett, F. R. Editors' Choice—Flooded by Success: On the Role of Electrode Wettability in CO2 Electrolyzers That Generate Liquid Products. *J. Electrochem. Soc.* **2020**, *167* (12), 124521. https://doi.org/10.1149/1945-7111/abaa1a.
(18) Corral, D.; Feaster, J. T.; Sobhani, S.; DeOtte, J. R.; Lee, D. U.; Wong, A. A.; Hamilton, J.; Beck, V. A.; Sarkar, A.; Hahn, C.; Jaramillo, T. F.; Baker, S. E.; Duoss, E. B. Advanced Manufacturing for Electrosynthesis of Fuels and Chemicals from CO2. *Energy Environ. Sci.* **2021**, *14* (5), 3064–3074. https://doi.org/10.1039/D0EE03679J.

(19) Wakerley, D.; Lamaison, S.; Ozanam, F.; Menguy, N.; Mercier, D.; Marcus, P.; Fontecave, M.; Mougel, V. Bio-Inspired Hydrophobicity Promotes CO2 Reduction on a Cu Surface. *Nat. Mater.* **2019**, *18* (11), 1222–1227. https://doi.org/10.1038/s41563-019-0445-x.
(20) Li, J.; Chen, G.; Zhu, Y.; Liang, Z.; Pei, A.; Wu, C.-L.; Wang, H.; Lee, H. R.; Liu, K.; Chu, S.; Cui, Y. Efficient Electrocatalytic CO2 Reduction on a Three-Phase Interface. *Nat. Catal.* **2018**, *1* (8), 592–600. https://doi.org/10.1038/s41929-018-0108-3.
(21) Leonard, M. E.; Orella, M. J.; Aiello, N.; Román-Leshkov, Y.; Forner-Cuenca, A.; Brushett, F. R. Editors' Choice—Flooded by Success: On the Role of Electrode Wettability in CO_2 Electrolyzers That Generate Liquid Products. *J. Electrochem. Soc.* **2020**, *167* (12), 124521. https://doi.org/10.1149/1945-7111/abaa1a.
(22) Hansen, K. U.; Jiao, F. Hydrophobicity of CO2 Gas Diffusion Electrodes. *Joule* **2021**, *5* (4), 754–757. https://doi.org/10.1016/j.joule.2021.02.005.
(23) Kim, B.; Hillman, F.; Ariyoshi, M.; Fujikawa, S.; Kenis, P. J. A. Effects of Composition of the Micro Porous Layer and the Substrate on Performance in the Electrochemical Reduction of CO2 to CO. *J. Power Sources* **2016**, *312*, 192–198. https://doi.org/10.1016/j.jpowsour.2016.02.043.
(24) Wicks, J.; Jue, M. L.; Beck, V. A.; Oakdale, J. S.; Dudukovic, N. A.; Clemens, A. L.; Liang, S.; Ellis, M. E.; Lee, G.; Baker, S. E.; Duoss, E. B.; Sargent, E. H. 3D-Printable Fluoropolymer Gas Diffusion Layers for CO_2 Electroreduction. *Adv. Mater.* **2021**, *33* (7), 2003855. https://doi.org/10.1002/adma.202003855.
(25) Goldman, M.; Krall, E.; Marufu, M.; Jue, M. L.; Tzintzun, S.; Wagner, J. K.; Jaffer, S.; Sarkar, A.; Fleischer, M.; Simon, E.; Wong, A. A.; Baker, S. E. Integration of Hydrophobic Gas Diffusion Layers for Zero-Gap Electrolyzers to Enable Highly Energy-Efficient CO2 Electrolysis to C2 Products. *Chem Catal.* **2025**, *5* (4), 101235. https://doi.org/10.1016/j.checat.2024.101235.
(26) Sisler, J.; Khan, S.; Ip, A. H.; Schreiber, M. W.; Jaffer, S. A.; Bobicki, E. R.; Dinh, C.-T.; Sargent, E. H. Ethylene Electrosynthesis: A Comparative Techno-Economic Analysis of Alkaline vs Membrane Electrode Assembly vs CO2–CO–C2H4 Tandems. *ACS Energy Lett.* **2021**, *6* (3), 997–1002. https://doi.org/10.1021/acsenergylett.0c02633.
(27) O'Brien, C. P.; McLaughlin, D.; Böhm, T.; Xiao, Y. C.; Edwards, J. P.; Gabardo, C. M.; Bierling, M.; Wicks, J.; Sedighian Rasouli, A.; Abed, J.; Young, D.; Dinh, C.-T.; Sargent, E. H.; Thiele, S.; Sinton, D. Scalability and Stability in CO2 Reduction via Tomography-Guided System Design. *Joule* **2024**, *8* (10), 2903–2919. https://doi.org/10.1016/j.joule.2024.07.004.
(28) Nelson, V. E.; O'Brien, C. P.; Edwards, J. P.; Liu, S.; Gabardo, C. M.; Sargent, E. H.; Sinton, D. Scaling CO2 Electrolyzer Cell Area from Bench to Pilot. *ACS Appl. Mater. Interfaces* **2024**, *16* (38), 50818–50825. https://doi.org/10.1021/acsami.4c11103.
(29) Goldman, M.; Krall, E.; Marufu, M.; Jue, M. L.; Tzintzun, S.; Wagner, J. K.; Jaffer, S.; Sarkar, A.; Fleischer, M.; Simon, E.; Wong, A. A.; Baker, S. E. Integration of Hydrophobic Gas Diffusion Layers for Zero-Gap Electrolyzers to Enable Highly Energy-Efficient CO2 Electrolysis to C2 Products. *Chem Catal.* **2025**, *5* (4), 101235. https://doi.org/10.1016/j.checat.2024.101235.
(30) Xiao, Y.; Yu, F.; Xia, C.; Zhu, D.; Chen, J.; Liu, N.; Zhao, Y.; Qi, R.; Guo, W.; You, B.; Yao, T.; Pang, Y.; Wang, Z.; Wang, H.; Song, F.; Xia, B. Y. Asymmetric CO–CHO Coupling over Pr Single-Atom Alloy Enables Industrial-Level Electrosynthesis of Ethylene. *J. Am. Chem. Soc.* **2025**, *147* (18), 15654–15665. https://doi.org/10.1021/jacs.5c02896.
(31) Fang, M.; Miao, X.; Huang, Z.; Wang, M.; Feng, X.; Wang, Z.; Zhu, Y.; Dai, L.; Jiang, L. Anionic Ionomer: Released Surface-Immobilized Cations and an Established Hydrophobic Microenvironment for Efficient and Durable CO2-to-Ethylene Electrosynthesis at High Current over One Month. *J. Am. Chem. Soc.* **2024**, *146* (39), 27060–27069. https://doi.org/10.1021/jacs.4c09168.

(32) Jeng, E.; Qi, Z.; Kashi, A. R.; Hunegnaw, S.; Huo, Z.; Miller, J. S.; Bayu Aji, L. B.; Ko, B. H.; Shin, H.; Ma, S.; Kuhl, K. P.; Jiao, F.; Biener, J. Scalable Gas Diffusion Electrode Fabrication for Electrochemical CO2 Reduction Using Physical Vapor Deposition Methods. *ACS Appl. Mater. Interfaces* **2022**, *14* (6), 7731–7740. https://doi.org/10.1021/acsami.1c17860.

Supplementary Information For "Through-Plane Conductive Hydrophobic Electrodes for CO_2 Electrolysis to Ethylene"

Eric Krall[1,2], Michell Marufu[1,2], Santiago TzinTzun[1,2,] Melinda L. Jue[1,2], Natalie Hwee[1,2], Shaffiq Jaffer[5], Amitava Sarkar[5,6], Herve Gross[5], Jonathan Raisin[5,6], Maximilian Fleischer[4], Elfriede Simon[4], Sarah Baker[1,2], Andrew A. Wong*[1,3] and Maxwell Goldman*[1,2]

[1]Materials Science Division, Lawrence Livermore National Laboratory, Livermore, CA, USA 94550

[2]Laboratory for Energy Applications for the Future, Lawrence Livermore National Laboratory, Livermore, CA, USA 94550

[3]Materials Engineering Division, Lawrence Livermore National Laboratory, Livermore, CA, USA 94550

[4]Innovation Department, Siemens Energy Global GmbH & Co. KG, Otto-Hahn-Ring 6, Munich 81739, Germany

[5]TotalEnergies Research & Technology USA, LLC, Houston, TX 77002, USA

[6]SUNCAT Center for Interface Science and Catalysis, Department of Chemical Engineering, Stanford University, Stanford, CA 94305, USA

*__Correspondence__: goldman23@llnl.gov, wong138@llnl.gov

Supplementary Tables

Table SI 1: Degree of crosslinking calculations of PFPE monomer resins using Flory-Stockmayer theory assuming 100% conversion and no significant chain transfer or termination.

PFPE (wt%)	PFPE (mol)	TPO-L (mol)	Sol Fraction	Gel Fraction (Degree of Crosslinking)
30	0.0015	0.000171	0.228	0.772
35	0.00175	0.000171	0.195	0.805
40	0.0020	0.000171	0.171	0.829

Table SI 2: Performance metrics for zero-gap CO_2 to ethylene demonstrations at scales >=25 cm^2

V full cell [V]	$FE_{ethylene}$ [%]	current density (A cm^{-2})	stability [h]	size [cm^2]	energy efficiency [%]	Ref
5	26	0.125	240	800	6.4	1
5	33	0.2	240	800	5.4	2
3.6	55	0.2	200	100	18.8	3
2.5	48	0.2	12	25	23.6	4
3.05	55	0.6	0	25	21.2	5
3.6	38	0.2	0	25	12.9	6

Supplementary Figures

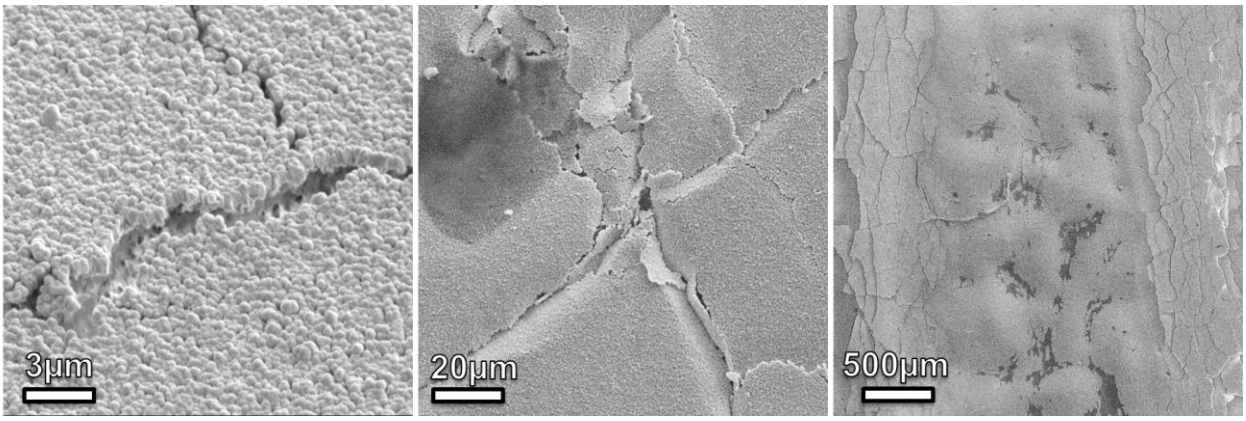

Figure SI 1. microporous PFPE polymer with high monomer loading (40 wt%) and 500nm catalyst coating, post compression

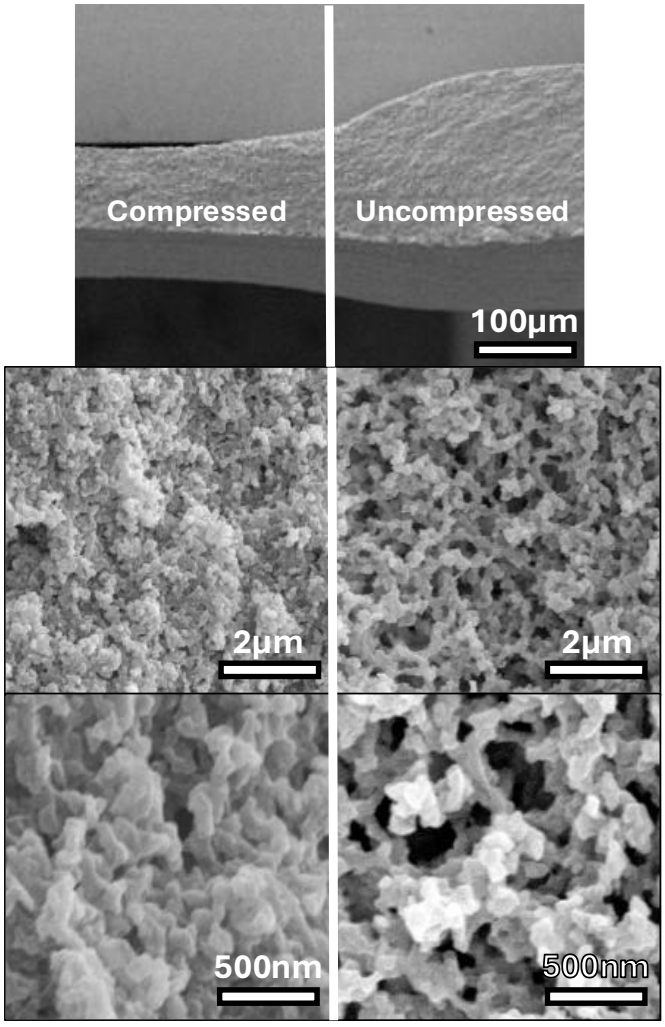

Figure SI 2. microporous PFPE polymer showing pore collapse post hot-press.

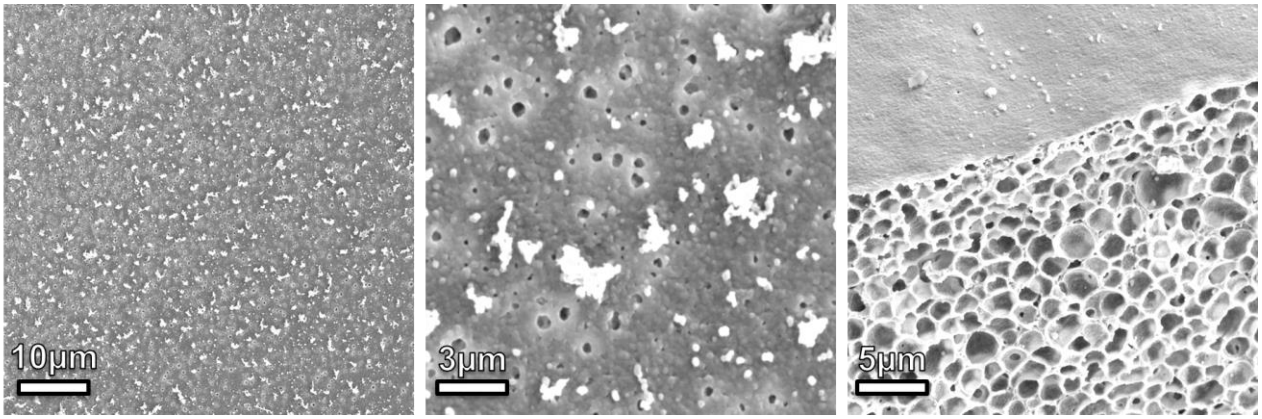

Figure SI 3. microporous PFPE polymer with high monomer loading (40 wt%) cured high light intensity (8 mW/cm^2)

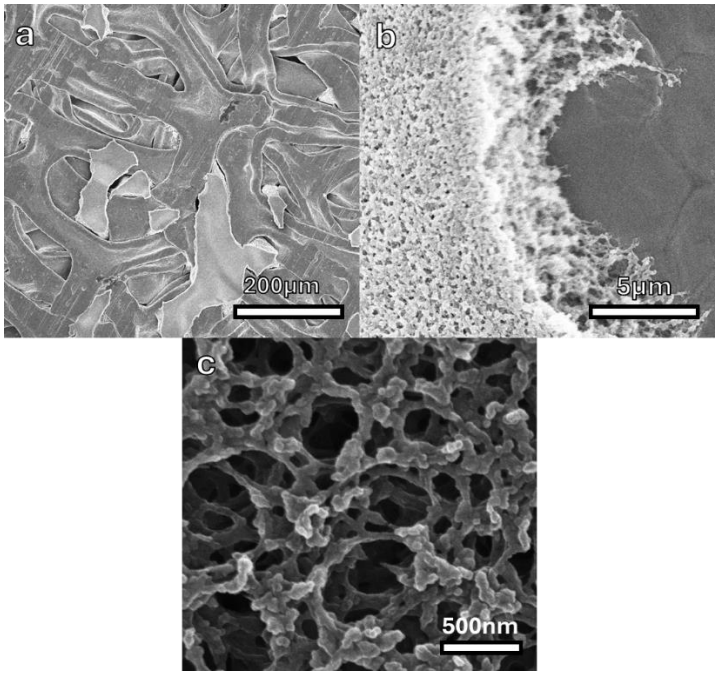

Figure SI 4. Micrographs of uncoated 35wt% composite GDE a) large area showing copper struts and PFPE fill, b) PFPE next to copper strut, c) zoomed in PFPE showing retention of porosity.

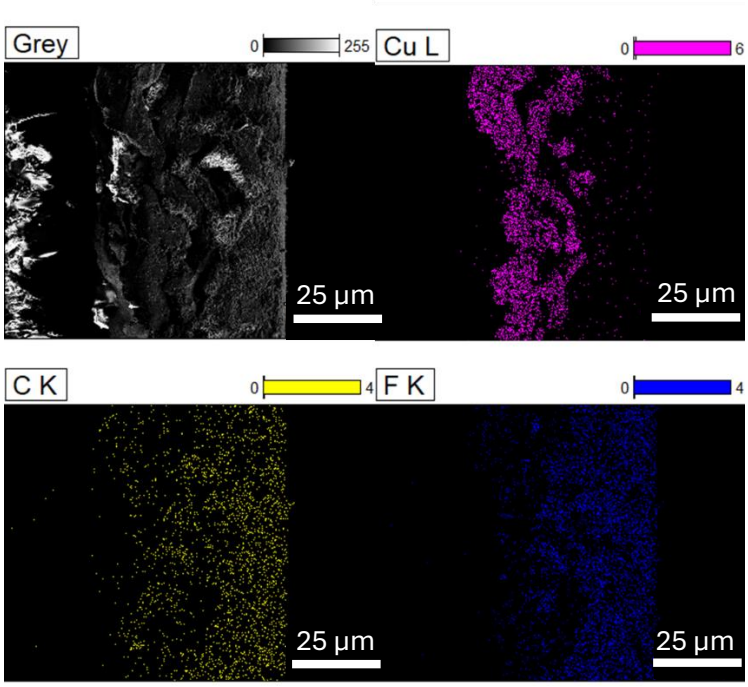

Figure SI 5. EDS cross section of composite GDE 10 minutes of exposure 10kV accelerating voltage.

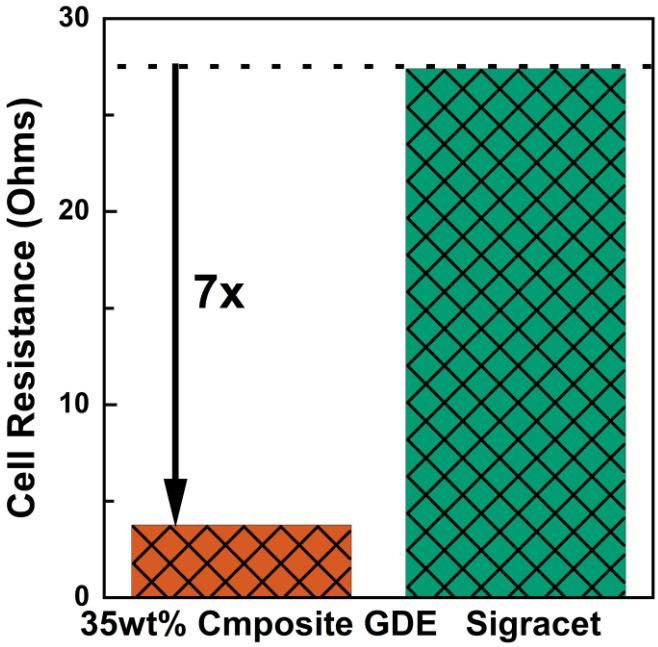

Figure SI 6. Full cell resistance copper coated (500nm) 35wt% composite GDE versus Sigracet carbon paper at 80% cell compression.

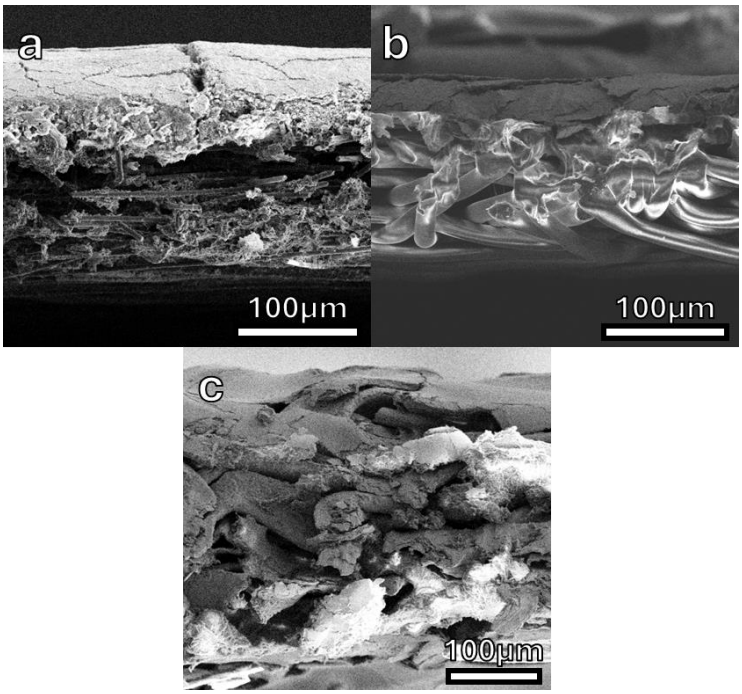

Figure SI 7. Cross section micrographs of Cu coated porous gas diffusion layers a) Sigracet 39BB, b) 0.45um ePTFE, c) 35 wt% composite GDE.

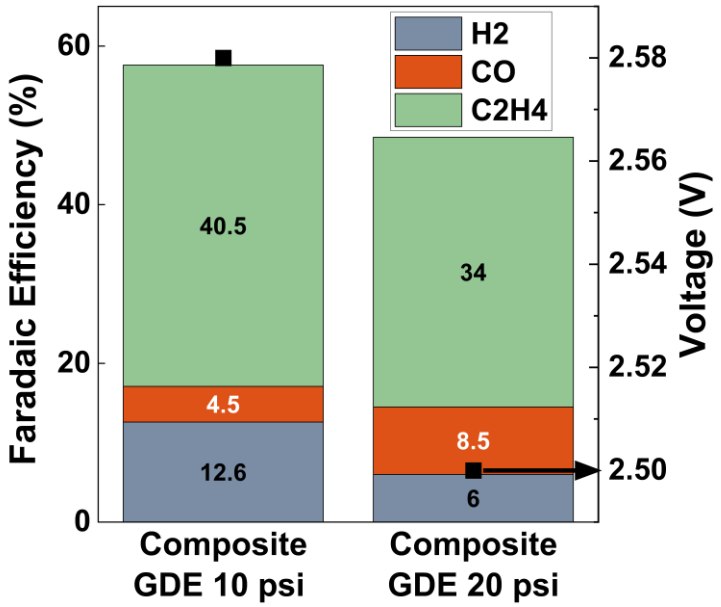

Figure SI 8. Gas products Faradaic efficiencies of a 25cm^2 35wt% composite GDE using 0.5M KOH

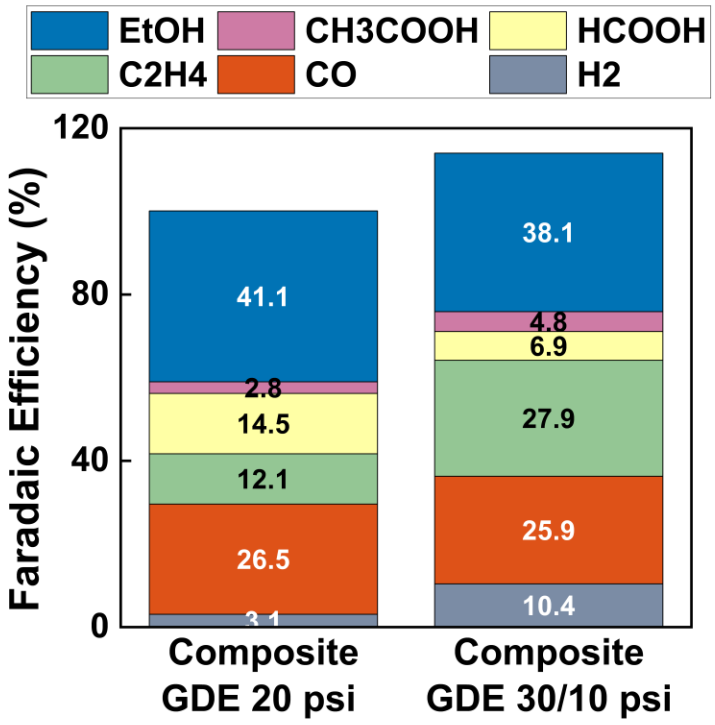

Figure SI 9. Product Faradaic efficiencies of a 100 cm2 35wt% Composite GDE in a zero-gap electrochemical cell.

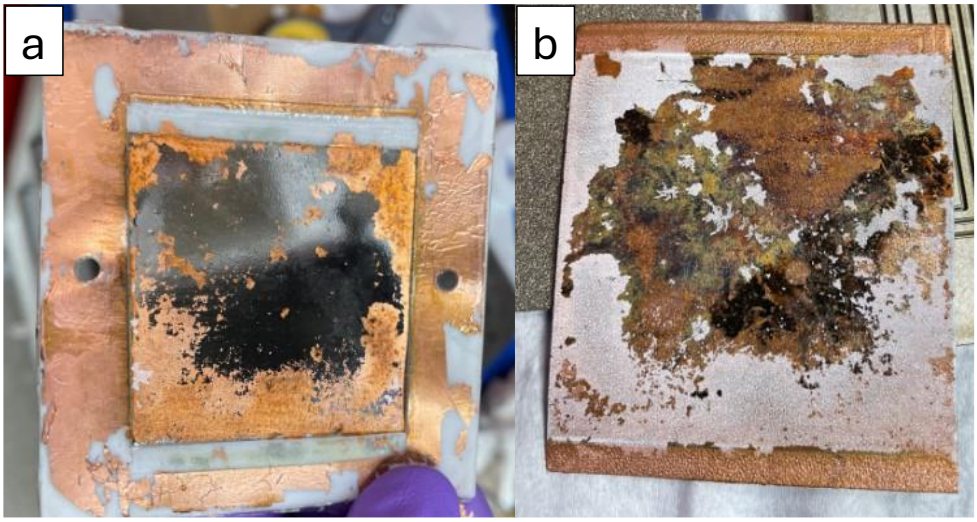

Figure SI 10. Cell disassembly after testing which results in transference of membrane to the cathode (a), and delamination of catalyst onto membrane (b).

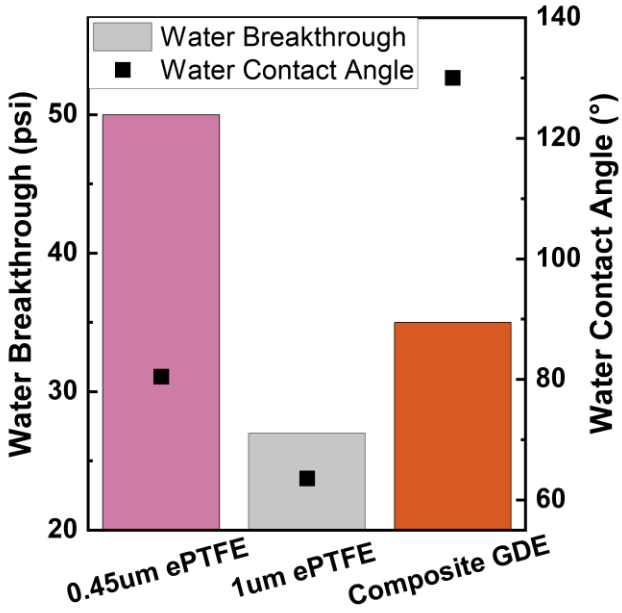

Figure SI 11. Water breakthrough pressure (psi) and water contact angle (°) of ePTFE samples versus composite GDE, all coated in 500nm Cu catalyst layer.

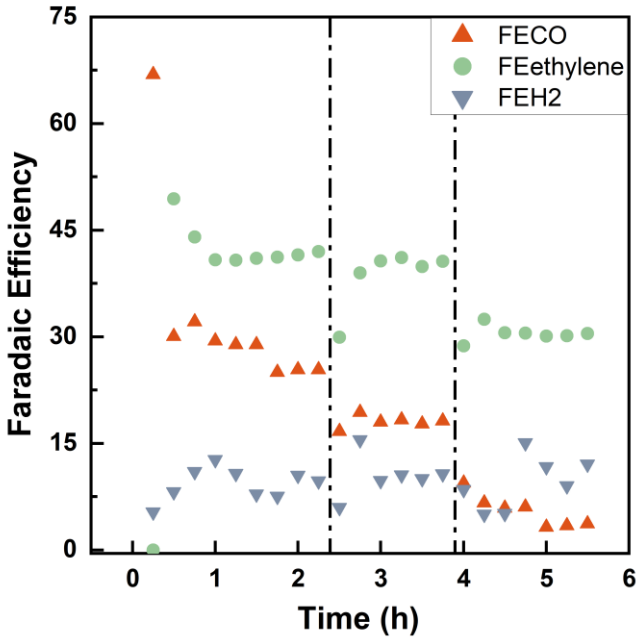

Figure SI 12. Gas product efficiencies of 100cm^2 0.45µm ePTFE after 2 anolyte swaps.

Supplementary Information

Section 1: Materials and Methods

1.1 Fabrication Methods

1.1.1 Gas Diffusion Electrode Fabrication

Copper Foam preparation

1.5 mm thick copper foam (M.T.I) is cut using a 36 cm^2 Apple Steel Rule Die and hot pressed at 300 °C with 22 tons of force for 3 minutes. It is then rotated 180 degrees and pressed again for another 3 minutes under the same conditions with a final thickness of approximately 0.16 mm. The samples are soaked in an acetone bath for thirty minutes to remove any contaminants.

PFPE resin formulation Preparation

Flurolink™ MD700 (3.5 g, Cornerstone Technology) is dissolved in dry N-Methyl-2-pyrrolidone (NMP, 4.5 g, Sigma-Aldrich) in a 20 mL scintillation vial. Triethylene glycol (TEG, 1.35 g, Sigma-Aldrich) is added and mixed until the opaque solution turns clear. An additional 0.45 g of TEG is added to the solution and again mixed until clear. The scintillation vial is then wrapped in aluminum foil, followed by the addition of ethyl 2,4,6-trimethylbenzoyl) phenylphosphinate (TPOL, 0.09 g, Rahn USA Corp). The solutions are stirred for 30 minutes at 50 RPM on an analog tube roller (SCILOGEX SCI-T6-S).

UV Curing Setup

An adjustable pull-out tray in an SPDI UV Exposure Lab Chamber is wrapped with aluminum foil. Two 37.5 mm-tall shell vials are placed in the middle of the adjustable tray. To alter the UV dosage, the curing bulbs are toggled on/off and pull-out tray is lowered/raised. Each formulation is cured with varying UV intensities, with each formulation receiving a total UV dose of 150 mJ. For a UV intensity of 0.5 mW cm^{-2} had a curing time of 300 seconds. A UV intensity of 2.5 mW cm^{-2} had curing time of 60 seconds. A UV intensity of 8 mW cm^{-2} had a curing time of 18.75 seconds

Sample Preparation and Processing

Both glass slides undergo treatment with an O_2 + Ar plasma at 100 W utilizing the PIE Scientific Tergeo-Plus Tabletop Plasma System. The larger slide (10 cm x 10 cm) is positioned on a flat, elevated surface, and approximately 2 grams of resin are poured onto it. A copper foam sample (6 cm x 6 cm) is subsequently placed atop the resin, followed by an additional 2 grams of resin to ensure complete coverage of the foam. The smaller slide (10 cm x 7 cm) is placed over the foam, starting from one end to the other, to mitigate bubble entrapment. The two slides are then secured together using two small binder clips before UV curing on top of vials to ensure light penetration.

The samples undergo a solvent exchange in an acetone bath, with the acetone replaced every thirty minutes, repeated three times. They are then moved to a critical point dryer, where they are submerged in acetone and separated by polypropylene spacers. The chamber temperature is cooled to 12 °C before liquid CO_2 is introduced into the chamber. Acetone is removed through the bottom release valve while the top release valve is periodically opened to release CO_2 gas. Once all the acetone is removed, the chamber is heated to 55 °C, and pressure is maintained between 1200-1,500

psi. Once the internal chamber reads 55 °C the top release valve is left slightly open until chamber pressure reaches atmospheric. The samples are then ready for copper catalyst coating.

Copper Catalyst Coating

For all catalyst preparations, a magnetron sputtering system (Kurt J. Lesker) was used to deposit thin films of Copper. The samples were taped (Kapton tape) on four sides to a 6 in. silicon wafer and pumped down to 1E−5 Torr before being loaded into the sputter chamber, fitted with a 99.999% purity copper target (Kurt J. Lesker). Ultra-high-purity argon (99.999%) was used for plasma generation with an ignition pressure of 15 mTorr and a working pressure of 3 mTorr. We pre-sputtered the target for 1 min prior to deposition to remove any native oxide before increasing the power of the DC magnetron sputtering system to 100 W and depositing 500 nm of Cu. The thickness was not monitored during the experiment; rather, a deposition rate was determined and confirmed with witness samples of silicon wafers masked with Kapton tape. Post-deposition sample thicknesses were verified by a profilometer (Bruker DektakXT).

Characterization:

Compression (Instron)

Adjustable spring-leveled attachment is installed to Instron and calibrated so that the head is parallel to the bottom plate. A 5cm^2 circle punch is used to cut out the sample and placed in the middle of the bottom plate. The plates are zeroed before compressing the sample to 1kN stopping force, and young's modulus is automatically calculated using the included Bluehill Universal software package.

Morphology (SEM)
Samples (~1cm^2) are cut out and adhered to a glass slide with double-sided copper tape. The samples, unless already coated with copper catalyst, are coated with ~20nm gold using a benchtop sputter coater (Cressington Sputter Coaters). The glass slide is adhered to a standard SEM pin holder (Ted Pella Inc.) using carbon tape to electrically ground samples. The samples are then ready for imaging and loaded into the chamber of an Apreo SEM (ThermoFisher) with accelerating voltage of 10kV and 0.1nA beam current.

Hydrophobicity (Contact Angle)

For all contact angle measurements, a Ramé-Hart model 500 advanced goniometer/tensiometer was used in conjunction with a U4 Series 520 fps SuperSpeed digital camera attached for all drop imaging. DROPimage Advanced was used for all image analyses. After calibrating the baseline and drop size on a blank silicon wafer, the samples were taped flat onto the sample stage with Kapton tape and leveled them prior to depositing 10 µL of DI water onto the sample surface. Left-side and right-side measurements were taken in triplicate on three independent portions of the sample and averaged manually before being reported.

Water breakthrough pressure and gas permeability

CO_2 permeation measurements were taken using a custom-built dead-end permeation system at ambient conditions (21 °C). GDL samples were cut from larger samples using a hammer-driven hole punch and mounted onto polyimide frames (127 µm thick Kapton® HN, DuPont) using silicone glue (734 Flowable Adhesive Sealant, Dow Corning). The upstream of the membrane was flushed several

times with CO_2 and allowed to come to equilibrium before measurement. The feed was pressurized up to 10 psi and the downstream flow rate was measured using mass flow meters.

The water breakthrough pressure was determined using a dead-end liquid permeation cell at ambient temperature (21 °C). GDL samples were cut from larger samples using a hammer-driven hole punch and placed in the permeation cell. 50 mL of deionized water was used as the feed and the cell was slowly pressured using N_2 gas. The first sign of water permeation on the downstream of the GDL was considered as the water breakthrough pressure.

Electrochemical testing

Anion exchange membranes (Sustainion™, X37-50 Grade RT) were prepared by cutting sheets sized to the anode and cathode blocks, soaking them in 1 M KOH (Sigma Aldrich) for at least 24 hours with the solution replaced after 5-8 hours. Prior to assembly, alignment holes were cut into the membrane using a hole punch. Ni foam (MTI Corporation, 1.6 mm thickness) was hot pressed for five minutes at 175 °F, 20,000 psi, resulting in a thickness of 10/1000". Electrolyte was prepared using MilliQ water and cesium hydroxide monohydrate (0.5 M, 1L) (Sigma Aldrich, >99.5% trace metal basis). Nickel foam is first placed on the anode facing upwards before a PTFE gasket of appropriate size (thickness and area) is then placed on top of the nickel foam. Carbon and titanium blocks printed each with a serpentine flow field (Fuel Cell Technologies Inc.) were utilized as the cathode and anode respectively. The flow field dimensions on each block were sized to the geometric surface area of the GDE. Each block also contained two pinholes to assist with alignment during assembly. Polytetrafluoroethylene (PTFE) gaskets (Grainger) were cut using a die press (Ace Steel Rule Dies) with holes sized to fit the area of the GDE. Electrolyte was prepared using MilliQ water and potassium hydroxide (Sigma Aldrich, ACS Reagent, ≥85% pellets). Fuel Cell Technologies Inc current collectors and electrolyzer housing were utilized. A torque wrench was used to tighten the screws (70 psi) to secure the assembly and adjust the assembly pressure. Carbon dioxide gas (Airgas, 99.999% purity) was used as received. Electrolyte was then circulated through the anode side of the MEA by connecting the anode side flow field to an electrolyte reservoir, while the flow rate was controlled using a diaphragm pump (Grundfos). Carbon dioxide gas was input through the cathode compartment and output to a gas chromatograph (SRI Instruments) using a mass flow controller (MKS Instruments) to control the rate of gas delivery. The flow rate was monitored and controlled using a mass flow meter (Agilent and Omega).

Electrolysis

Electrolysis experiments were conducted in a two-electrode setup and controlled using a Biologic potentiostat (VSP-3e) configured with a booster (VMP 3B-20). Unless otherwise stated, electrolysis experiments were conducted at two current densities 100 and 200 mA cm^{-2}. Gas products were quantified using inline gas chromatography, set to inject gas sample in 15 minutes intervals. Electrolyte reservoir was exchanged with fresh potassium hydroxide solution to maintain pH >13 at the anode to prevent Ni dissolution, and liquid products were aliquoted for analysis via high-performance liquid chromatograph (HPLC, Agilent).

Gaseous products quantification

Gas chromatography (GC) was performed to detect CO2RR products such as CO, CH_4, and C_2H_4 along with H_2 from the parasitic HER using an SRI GC 8610C MG#5 with a flame ionization detector (FID) and a thermal conductivity detector (TCD). A 3' MolSieve column was used to separate H_2 and CO from the gas mixture in tandem with 6' HaySep D column to separate the remaining gases- CO_2, CH_4, and C_2H_4. N_2 (research grade) was used as the carrier gas at 15 psi. H_2 (research grade) was set to 20 psi along with internal compressed air at 5 psi to ignite the flame for FID to detect hydrocarbons. A temperature profile was set for fast separation of the gaseous products starting with 50 °C for 4.5 mins and then a temperature ramp to 200 °C for 5.5 mins. A total runtime of 10 mins with 5 mins of cooldown time for GC was used for continuous measurements during the electrochemical experiments.

Liquid products quantification

After each two-hour electrochemical experiment, 10 ml of the electrolyte was sampled for post-electrolysis liquid product detection and quantification using an Agilent Infinity 1290 II HPLC Formate (formic acid), acetate (acetic acid), and ethanol were detected using this instrument. The HPLC incorporated a Biorad Aminex column to specifically separate organic acids and alcohols. The products were detected using a refractive index detector (RID) with a sampling rate of 4 Hz and a diode array detector (DAD) set at 210 nm. An isocratic elution flow rate of 0.5 ml/min was maintained for the mobile phase of milli Q water. The column temperature was 60 °C and the RID temperature was 35 °C. A 40 μl of the sample was injected into the column using the instrument's autosampler. The autosampler needle drive speed was set to 5 $\mu l/s$ for the sample intake from the vials, and the ejection drive speed was set to 10 $\mu l/s$. The products were analyzed for a retention time of 40 mins.

Acknowledgements

M.G., E.K., M.M., M.J., S.T., N.H., A.A.W., S.B. acknowledge financial support from TotalEnergies SE, and Siemens-Energy SE. This material is based upon work supported by the U.S. Department of Energy's Office of Energy Efficiency and Renewable Energy (EERE) under the Advanced Manufacturing Office (AMO) funding opportunity announcement DE-FOA-0002252. E.K., M.M., S.T., M.J., N.H., S.B., A.A.W., M.G contributed under the auspices of the US Department of Energy by Lawrence Livermore National Laboratory under contract DE-AC52-07NA27344 within CRADA TC02449, IM: LLNL-JRNL-2011466

References

(1) O'Brien, C. P.; McLaughlin, D.; Böhm, T.; Xiao, Y. C.; Edwards, J. P.; Gabardo, C. M.; Bierling, M.; Wicks, J.; Sedighian Rasouli, A.; Abed, J.; Young, D.; Dinh, C.-T.; Sargent, E. H.; Thiele, S.; Sinton, D. Scalability and Stability in CO2 Reduction via Tomography-Guided System Design. *Joule* **2024**, *8* (10), 2903–2919. https://doi.org/10.1016/j.joule.2024.07.004.

(2) Nelson, V. E.; O'Brien, C. P.; Edwards, J. P.; Liu, S.; Gabardo, C. M.; Sargent, E. H.; Sinton, D. Scaling CO2 Electrolyzer Cell Area from Bench to Pilot. *ACS Appl. Mater. Interfaces* **2024**, *16* (38), 50818–50825. https://doi.org/10.1021/acsami.4c11103.

(3) Xiao, Y.; Yu, F.; Xia, C.; Zhu, D.; Chen, J.; Liu, N.; Zhao, Y.; Qi, R.; Guo, W.; You, B.; Yao, T.; Pang, Y.; Wang, Z.; Wang, H.; Song, F.; Xia, B. Y. Asymmetric CO–CHO Coupling over Pr Single-Atom Alloy Enables Industrial-Level Electrosynthesis of Ethylene. *J. Am. Chem. Soc.* **2025**, *147* (18), 15654–15665. https://doi.org/10.1021/jacs.5c02896.

(4) Goldman, M.; Krall, E.; Marufu, M.; Jue, M. L.; Tzintzun, S.; Wagner, J. K.; Jaffer, S.; Sarkar, A.; Fleischer, M.; Simon, E.; Wong, A. A.; Baker, S. E. Integration of Hydrophobic Gas Diffusion Layers for Zero-Gap Electrolyzers to Enable Highly Energy-Efficient CO2 Electrolysis to C2 Products. *Chem Catalysis* **2025**, *5* (4), 101235. https://doi.org/10.1016/j.checat.2024.101235.

(5) Fang, M.; Miao, X.; Huang, Z.; Wang, M.; Feng, X.; Wang, Z.; Zhu, Y.; Dai, L.; Jiang, L. Anionic Ionomer: Released Surface-Immobilized Cations and an Established Hydrophobic Microenvironment for Efficient and Durable CO2-to-Ethylene Electrosynthesis at High Current over One Month. *J. Am. Chem. Soc.* **2024**, *146* (39), 27060–27069. https://doi.org/10.1021/jacs.4c09168.

(6) Jeng, E.; Qi, Z.; Kashi, A. R.; Hunegnaw, S.; Huo, Z.; Miller, J. S.; Bayu Aji, L. B.; Ko, B. H.; Shin, H.; Ma, S.; Kuhl, K. P.; Jiao, F.; Biener, J. Scalable Gas Diffusion Electrode Fabrication for Electrochemical CO2 Reduction Using Physical Vapor Deposition Methods. *ACS Appl. Mater. Interfaces* **2022**, *14* (6), 7731–7740. https://doi.org/10.1021/acsami.1c17860.